Field-effect induced tunability in hyperbolic metamaterials

Georgia T. Papadakis and Harry A. Atwater

Phys. Rev. B **92**, 184101 — Published 2 November 2015

DOI: 10.1103/PhysRevB.92.184101

Field effect-induced tunability in hyperbolic metamaterials

Georgia T. Papadakis[1,†] and Harry A. Atwater[1]

[1] Thomas J. Watson Laboratories of Applied Physics, California Institute of Technology, California 91125, USA

[†]Corresponding author e-mail: gpapadak@caltech.edu

Abstract

We demonstrate that use of the field effect enables tuning of the effective optical parameters of a layered hyperbolic metamaterial at optical frequencies. Field effect gating electrically modulates the permittivity in transparent conductive oxides via changes in the carrier density. These permittivity changes lead to active modulation of the effective electromagnetic parameters along with active control of the anisotropic dispersion surface of hyperbolic metamaterials and enable the opening and closing of photonic band gaps. Tunability of effective electric permittivity and magnetic permeability also leads to topological transitions in the optical dispersion characteristics.

Keywords

Hyperbolic metamaterials (HMM), isofrequency contour, density of optical states, epsilon near zero (ENZ), epsilon near pole (ENP), field effect, transparent conductive oxide (TCO), indium tin oxide (ITO), metal-oxide-semiconductor (MOS)

I. INTRODUCTION

Over the past decade, extensive study of optical metamaterials, artificial materials composed of sub-wavelength nanostructures, has revealed light-matter interactions unseen in the natural world. Their exotic properties arise from engineering their effective electromagnetic parameters, namely, their effective electric permittivity and magnetic permeability, to be markedly different from those of natural materials. Recently, epsilon near zero (ENZ) [2, 3] and mu near zero [4] metamaterials have been reported as slow-light media, negative index materials that enable super-resolution imaging[5,6] have been demonstrated and high-index metamaterials for sub-diffraction imaging[7] have been investigated. Hyperbolic metamaterials are a special class of metamaterials with uniaxial anisotropy and effective parameters of opposite signs along different coordinate directions [8, 9]. Such systems are being intensively studied because they exhibit diverging density of states, enabling extreme Purcell factors to be achieved [10], and support negative refraction of power [8]. They are also being investigated for emissivity control engineering for solar energy applications [11, 12]. The range of fundamental phenomena and applications achievable by metamaterials can be significantly expanded by actively tuning their effective electromagnetic parameters to enable dynamic control over their optical response. Such active control over metamaterials intrinsic properties can pave the way towards novel active optical components like holographic displays, improvement of LCD technology with solid-state materials, tunable polarizers, sensors and switches, slow-light media and optical memories.

Tuning the effective electromagnetic parameters of metamaterials also leads to active control over their dispersion characteristics. The past decade has revealed a plethora of new phenomena in electronic materials in condensed matter physics, but also in their photonic counterparts, arising from engineering their electronic band structure and photonic dispersion surface respectively. Classical phenomena such as Lifshitz transitions [13] and Van Hove singularities that lead to extreme values of

magnetoresistance arise from inducing transitions in the Fermi surface of electronic systems. Quantum-mechanical effects such as those arising from Dirac-like dispersion surfaces, leading to topological Dirac phases are the result of band structure engineering, leading to three-dimensional semimetals [14] and topological insulators [15]. Photonic analogues of topological insulators, in other words photonic materials that support non-trivial topologically protected states against back-scattering, have been realized with helical waveguides in a honeycomb lattice [16], by engineering the dispersion characteristics of photonic crystals. Theoretical studies suggest other configurations for realization of such protected states like chiral metamaterials with equal values of electric permittivity and magnetic permeability [17], or with chiral hyperbolic metamaterials [18] or with index-near-zero (which can be generalized to effective electric permittivity or magnetic permeability near-zero) metamaterials [19, 20]. The latter idea arises from the consideration that Dirac-like dispersion cones can be realized in a linear dispersion regime where the metamaterial effective parameters approach zero, allowing for topological transitions to occur in metamaterials. Hyperbolic metamaterials also support ENZ and epsilon near pole (ENP) spectral regions [1, 21] that induce band splitting and support such topological transitions [22]. Thus, active tuning of the effective parameters can tune the spectral regions of topological transitions along with the possibility to dynamically study topological transitions in photonic systems.

Recent studies on tunable metamaterials focusing in the infrared-THz spectral range have investigated graphene as a tunable material to effectively realize a tunable hyperbolic dispersion. The mechanism for tunable metamaterial response by variation of the conductivity of grapheme monolayers has been theoretically studied in [23, 24] and [25]. In these studies, the carrier densities in effective capacitor configurations comprised of adjacent graphene layers separated by dielectric materials are modulated by carrier injection through an applied voltage that actively modulates the Fermi level. Other mechanisms have also been studied, for example application of external DC magnetic fields to modulate the spatial dispersion of effective electric permittivity of hyperbolic metamaterials [26].

In this work we focus in the optical regime and we find that electrical gating of transparent conductive oxide (TCO) based metamaterials leads to significant tuning of their optical response, whose governing physics is different from graphene-based structures in the IR [23, 24,25]. This approach has potential to yield a power-efficient tunable visible frequency hyperbolic metamaterial with ultrafast (~fs) modulation that is robust and compatible with current optical technology. Potential tuning mechanisms include modifying the complex dielectric function of component materials via phase transitions [27], mechanical deformations [28] as well as electronic mechanisms [29, 30] for tuning such as carrier accumulation and depletion [31]. Among these, field effect modulation is particularly attractive because of its robustness and very low power dissipation in steady state. It has recently been investigated for optical modulators [32-36] by using the spectral tunability of the electronic properties in transparent conductive oxides or transition-metal nitrides [37] for modulating the modal effective index in waveguide configurations.

Here we investigate the effects of carrier density changes in TCO accumulation layers on the effective electromagnetic optical parameters of hyperbolic metamaterials. We study a frequency and dispersion-tunable hyperbolic metamaterial (HMM) with field effect gating to electrically modulate the permittivity in conductive oxides layers. We find that such modulation induces drastic changes in the metamaterial dispersion surface. Actively controlled transitions between regions of hyperbolic dispersion and band gap regions are identified as a topological transitions of the dispersion surface [22], leading to singularities in the density of optical states. We calculate the effective electric permittivity and magnetic permeability tensors of the HMM and we show that active permittivity modulation can be as high as

200% for experimentally realizable geometries and TCOs. This also results in tunability of the effective birefringence and dichroism of the metamaterial and in tunability of its photonic band gaps. By performing exact electromagnetic parameter retrieval calculations instead of the use of an effective medium approximation we reveal electrically tunable magnetic parameters. We perform a sensitivity analysis of the electronic properties of the TCO, to provide insight for practical realization of tunable HMMs with various conductive oxides and degenerately doped semiconductors. The design simplicity and robustness of field effect modulation, similar to structures now pervasive in CMOS electronics, opens the door to widespread applications in future optical technologies.

II. TUNABLE PLANAR HYPERBOLIC METAMATERIAL: THE CONCEPT

A hyperbolic metamaterial can be realized in a stack of metal-dielectric multilayers with sub-wavelength thicknesses. It is characterized through a tensorial electric permittivity $\vec{\varepsilon} = diag(\varepsilon_{xx},\varepsilon_{yy},\varepsilon_{zz}) = diag(\varepsilon_o,\varepsilon_o,\varepsilon_e)$ and magnetic permeability $\vec{\mu} = diag(\mu_{xx},\mu_{yy},\mu_{zz}) = diag(\mu_o,\mu_o,\mu_e)$, where ε_o and μ_o refer to the ordinary parameters in the in-plane direction, while ε_e and μ_e correspond to the direction of the optical axis. The strong anisotropy along the optical axis causes the TM polarized bulk modes, containing an electric field component in this direction, to experience strong birefringence expressed via the dispersion equation[1]:

$$\frac{k_x^2 + k_y^2}{\varepsilon_e \mu_o} + \frac{k_z^2}{\varepsilon_o \mu_o} = k_o^2 \qquad (1)$$

Recent studies [1, 21] have shown that planar HMMs can be engineered to exhibit hyperbolic dispersion of type I ($\mathrm{Re}(\varepsilon_e\mu_o) < 0$ and $\mathrm{Re}(\varepsilon_o\mu_o) > 0$) and type II ($\mathrm{Re}(\varepsilon_e\mu_o) > 0$ and $\mathrm{Re}(\varepsilon_o\mu_o) < 0$), in addition to regions where propagation is forbidden due to simultaneously negative values of the denominators in Eq. 1. By introducing a TCO within the unit cell of a metal/dielectric metamaterial, as shown in Fig. 1, and actively modulating the carrier density through application of a DC bias across the metal/TCO layers, an accumulation layer is formed at the dielectric/TCO interface, shown with light blue color in Fig. 1.

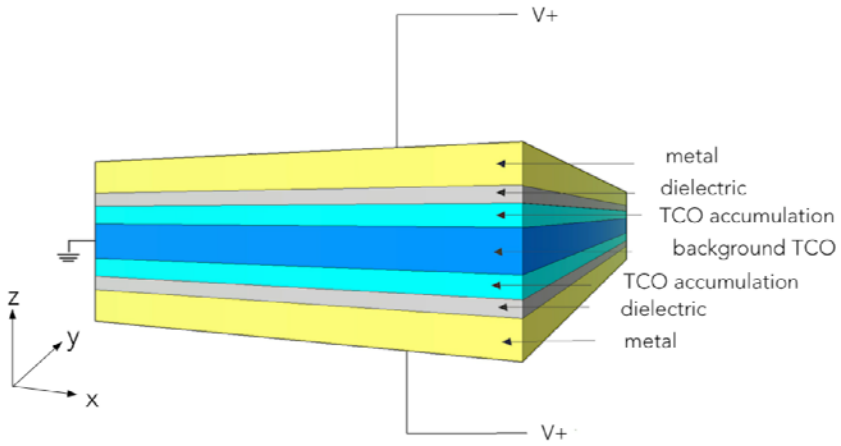

Fig.1: Schematic of a unit cell of a tunable planar metamaterial.

This changes Maxwell's boundary conditions on those interfaces, which affects the effective

metamaterial parameters, which are obtained through a parameter retrieval method [1]. The optical parameter affected the most through this modulation is the extraordinary permittivity ε_e as we show in Part B. This influences the metamaterial band structure, birefringence and dichroism. Prior to investigating a specific unit cell, we discuss possible dielectrics and TCOs that can potentially be implemented in a tunable HMM unit cell like the one shown in Fig. 1. Specifically, for inducing strong tunablility, we investigate high-strength dielectrics for sustaining large breakdown fields and TCOs with high background carrier concentrations that give rise to plasma frequencies in the near-IR regime.

A. ELECTRONIC PROPERTIES: HIGH-STRENGTH DIELECTRICS AND TCOs

Ignoring detailed band bending effects, to first order, charge carrier accumulation can be schematically modeled via a uniform layer with increased carrier concentration relative to the background TCO, with thickness given by the Debye length d. A simple electrostatic calculation on a metal/dielectric/TCO interface, as depicted in Fig. 1, dictates that:

$$\frac{V}{t} = \frac{|e|Nd}{k_{diel}\varepsilon_o} \leq E_{br} \tag{2}$$

where V is the applied bias between the metal and TCO, t is the thickness of the dielectric, k_{diel} is the DC dielectric constant of the dielectric, ε_o is the vacuum permittivity and E_{br} is the breakdown field of the dielectric material. N is the carrier density in the accumulation layer. To achieve tunability of the effective parameters within the visible regime, the TCO incorporated into the metamaterial design must have a plasma frequency within the IR-visible spectrum. This corresponds to a high background carrier concentration of the order $10^{19} - 10^{21} / cm^3$ and it dictates the use of dielectric materials with high electrical breakdown fields.

The TCO we investigate in this work is indium tin oxide (ITO), which has been studied extensively in the literature [32, 33, 38-41]. We model ITO with a Drude model, which provides an adequate and accurate description of its permittivity in the visible-IR regime [32, 33, 39, 41, 42]. ITO can be heavily doped using rf sputter deposition, yielding a carrier concentration in the range $10^{19} - 10^{21} / cm^3$ with a plasma frequency in the infrared range. Following previous experimental results [32, 33, 39, 43], we investigate here ITO with background carrier concentration of $5 \times 10^{20} / cm^3$. Active tunability of the carrier concentration of ITO in metal-oxide-semiconductor (MOS) structures by up to two orders of magnitude has been reported previously [32,33,34, 40, 41]. The results presented here are also relevant for other TCOs like aluminum doped zinc oxide (AZO) [38], gallium doped zinc oxide (GZO) [36, 38] or transition-metal nitrides [37] and degenerately doped semiconductors [35], as illustrated by a sensitivity analysis on the material electronic properties of the active layer discussed in Part II, C.

Table I illustrates the maximum achievable carrier concentration in the accumulation layer of ITO, for various dielectric materials whose breakdown fields have been reported: SiO_2, Al_2O_3, HfO_2 and $HfSiO_4$. Different Debye lengths d for the ITO are also considered, consistent with the range of parameters observed in previous experimental results [32-34, 40].

dielectric	E_b and and k_{diel}	N (in cm^{-3}), d=0.5nm	N (in cm^{-3}), d=1nm	N (in cm^{-3}), d=2.5nm	N (in cm^{-3}), d=5nm
SiO_2	E_b=[30-40] MV/cm [44] k_{diel}=3.9 [44-46]	[1.29-1.7]x10^{22}	[6.47-8.63]x10^{21}	[2.59-3.45]x10^{21}	[1.29-1.73]x10^{21}
Al_2O_3	E_b=[6-8] MV/cm [45, 47, 48] k_{diel}=9 [45, 46]	[5.97-7.96]x10^{21}	[2.99-3.98]x10^{21}	[1.19-1.59]x10^{21}	[5.97-7.96]x10^{20}
Al_2O_3	E_b=[6-8] MV/cm [45, 47, 48] k_{diel}=10.3 [48]	[6.83-9.12]x10^{21}	[3.42-4.56]x10^{21}	[1.37-1.82]x10^{21}	[6.84-9.12]x10^{21}
HfO_2	E_b=[40-60] MV/cm [44] k_{diel}=17 [44]	[7.52-11.28]x10^{22}	[3.76-5.64]x10^{22}	[1.5-2.26]x10^{22}	[7.52-11.28]x10^{21}
HfO_2	E_b=[40-60] MV/cm [44] k_{diel}=25 [46]	[11.1-16.6]x10^{22}	[5.53-8.23]x10^{22}	[2.21-3.32]x10^{22}	[1.11-1.66]x10^{22}
HfO_2	E_b=5.6 MV/cm [48] k_{diel}=18.7 [48]	1.55x10^{22}	7.74x10^{21}	3.09x10^{21}	1.55x10^{21}
$HfSiO_4$	E_b=10 MV/cm [46, 49] k_{diel}=11 [46, 49]	1.22x10^{22}	6.08x10^{21}	2.43x10^{21}	1.22x10^{21}
$HfSiO_4$ (with SiO_2)	E_b=10 MV/cm [46, 49] k_{diel}=[4.8-5.4] [50]	[5.31-5.97]x10^{21}	[2.66-2.99]x10^{21}	[1.06-1.19]x10^{21}	[5.31-5.97]x10^{20}
$HfSiO_4$ (with HfO_2)	E_b=10 MV/cm [46, 49] k_{diel}=[12.5-15.1] [50]	[1.38-1.67]x10^{22}	[6.91-8.35]x10^{21}	[2.77-3.34]x10^{21}	[1.38-1.67]x10^{20}

Table.1: Maximum achievable carrier concentration in ITO accumulation layers for reported values of breakdown field and DC dielectric constants of high-strength dielectrics

Good high-k dielectric quality is important for sustaining high carrier concentrations at the accumulation layer of ITO and, in turn, provides large tunability of the effective parameters of a planar HMM. HfO_2 is a particularly attractive dielectric for modulation of carrier density in a field-effect tunable metamaterial unit cell due to its simultaneously large values of DC dielectric constant [44, 46, 48,50, 51], and its high breakdown field. C. Sire et al. [44] have achieved breakdown fields as high as 40-60MV/cm, but the electrode geometry and area utilized in these experiments (AFM tip) is not typical of larger-area field effect devices. Y. H. Kim et al. have obtained breakdown fields as high as 36MV/ cm [52] for large-area (up to 100 micron x 100 micron) planar field effect electrode geometries while values in the range $5-10 MV/cm$ have been broadly reported in the literature [53, 54, 55 , 56].

B. A 'TOY' MODEL: RESULTS

We consider a unit cell of a HMM consisting of two 20 nm Ag layers separated by a 15 nm layer of ITO. The two materials are isolated from each other by 10 nm HfO_2 dielectric layers, as shown in Fig. 1. The thickness of HfO_2 has been chosen to correspond to thicknesses routinely achievable in atomic layer deposition [47, 48]. The refractive index of Ag has been measured by ellipsometry (See Supplemental Material Fig. S1 [57]) while the Sellmeier equation with three poles was used for the refractive index of HfO2 [58]. Under applied bias between the Ag and the ITO in the geometry of Fig. 1, we consider a 2.5nm accumulation layer to be formed in the HfO_2-ITO interface [32-34]. In Part II, C, we perform a sensitivity analysis over the accumulation layer thickness and maximum carrier density modulation in order to comprehensively assess the tunability range for this design for various TCOs or degenerate semiconductors and high-k dielectrics. We model both the background ITO and the accumulation layer using the Drude model with different carrier concentration, based on previous experimental results [32, 33, 39, 40] (See Supplemental Material Fig. S2 [57]).

The drastic change in the carrier concentration across the ITO background and accumulation

layer yields tunable optical parameters. We use a parameter retrieval method [1] to calculate the effective optical parameters ε_o, μ_o and ε_e and μ_e of this motif for increasing carrier concentration in the accumulation layer of ITO. The retrieved parameters are local and thus independent of the number of unit cells (See Appendix-Fig. A1). In order to verify the accuracy of our retrieval results, we also perform a Bloch wave-vector calculation using the image parameter method [59]. Comparison between the dispersion characteristics in the Bloch wave analysis and the retrieved wave-vectors can be found in the Appendix (See Figs. A2, A3, A4).

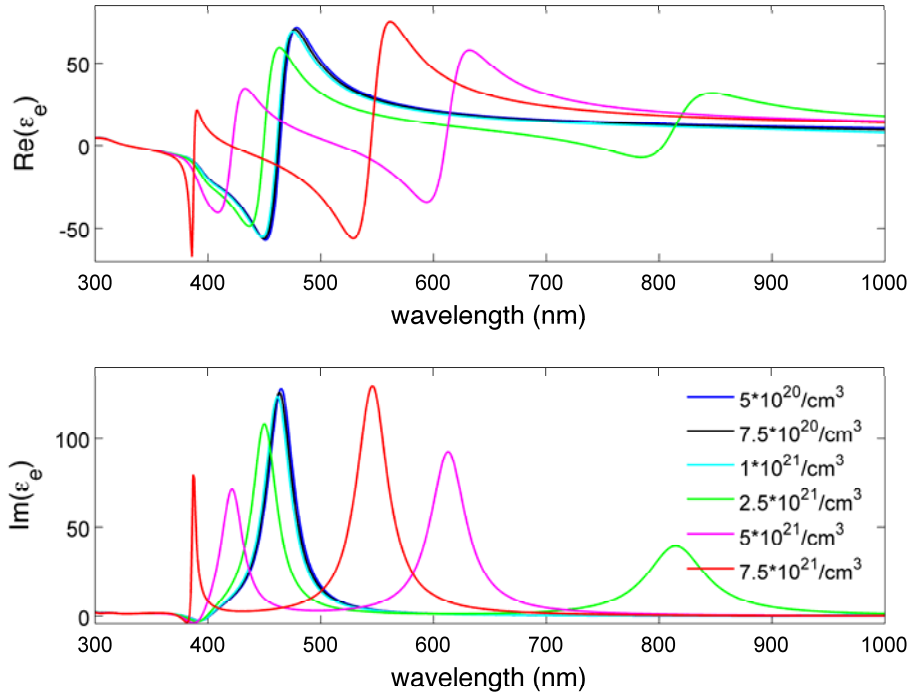

Fig. 2: Tunable effective extraordinary permittivity for various carrier concentrations in the accumulation layer

As the carrier concentration in the accumulation layer of ITO increases under applied bias from the background value of $5\times10^{20}/cm^3$ up to $7.5\times10^{21}/cm^3$, corresponding to experimentally reported carrier concentration changes [32], the Lorentzian-shaped resonance in extraordinary permittivity ε_e blue-shifts as seen in Fig. 2. This resonance arises form the coupling of the plasmonic modes supported on the metal/dielectric interfaces to the bulk high-k modes of the HMM [21]. The epsilon-near-pole (ENP) wavelength of this dominant resonance blue-shifts under applied bias by more than 60nm while remaining within the visible regime. More importantly, as depicted in Fig. 2, the application of a DC bias across the metamaterial layers also leads to the appearance of a secondary resonance, originating from the large increase in the charge density in the ITO accumulation layer.

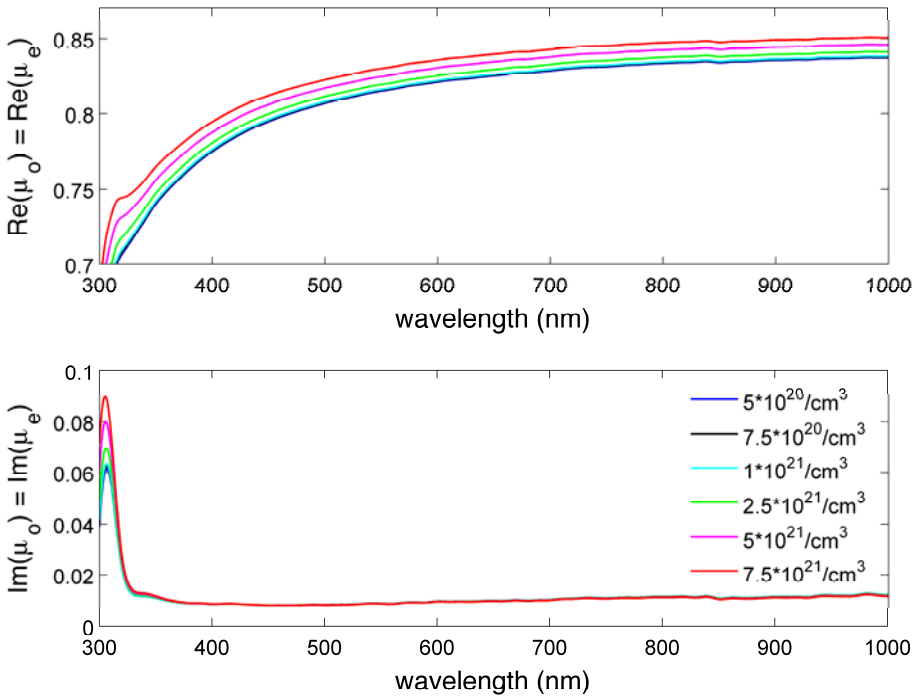

Fig. 3: Tunable effective extraordinary permeability for various carrier concentrations in the accumulation layer

The HMM unit cell exhibits a strong and broadband diamagnetic response. One of the most diamagnetic of natural materials is bismuth with a DC permeability of 0.999834 while the present metamaterial design enables permeability values of the order of 0.85 in the optical regime. This is a consequence of Lenz's law: the tangential component of the magnetic field induces a surface current at the interfaces of the multilayer, creating a magnetic response opposing the applied magnetic field. The magnetic permeability, which is isotropic, i.e $\mu_o = \mu_e$, is also noticeably tunable, as shown in Fig. 3. Since this HMM is magnetically isotropic, the TE polarized bulk modes do not experience an anisotropy since they are only affected by the ordinary permittivity ε_o, which is known to be metallic-like in planar HMMs [1]. The retrieved ε_o is not significantly tunable with variation of carrier concentration (See Fig. A5 in Appendix) since the in-plane response of this HMM is dominated by Ag layers rather than tunable ITO accumulation layers.

By contrast, the TM polarized bulk modes experience a strong anisotropy. According to Eq. 1, their effective birefringence and dichroism are defined as $\mathrm{Re}(\sqrt{\varepsilon_o \mu_o}) - \mathrm{Re}(\sqrt{\varepsilon_e \mu_o})$ and $\mathrm{Im}(\sqrt{\varepsilon_o \mu_o}) - \mathrm{Im}(\sqrt{\varepsilon_e \mu_o})$ respectively and are presented in Fig. 4 for increasing carrier concentration in the accumulation layer of ITO. As expected, HMMs exhibit extreme anisotropies, which is manifest in the large birefringence values shown in Fig. 4; these by far exceed the birefringence of the most anisotropic natural materials like liquid crystals and other uniaxial inorganic crystals (c.f., table in Fig. 4). Notable here is the broadband tunability of both birefringence and dichroism across the whole visible spectrum.

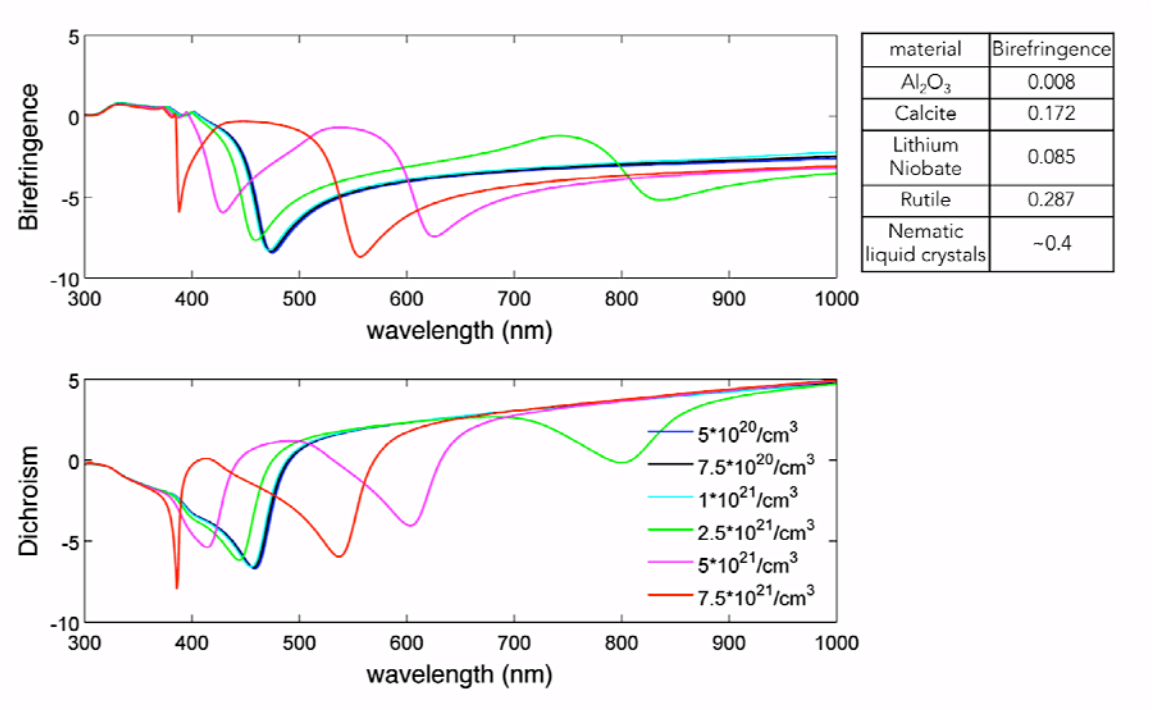

material	Birefringence
Al_2O_3	0.008
Calcite	0.172
Lithium Niobate	0.085
Rutile	0.287
Nematic liquid crystals	~0.4

Fig. 4: Tunable effective birefringence and dichroism

The tunability of the effective parameters presented in Figs. 2 and 3 has an effect on the dispersion surface for the TM waves, given by Eq. (1). This is demonstrated in Fig.5a, depicting the figure of merit defined as $FOM = \dfrac{\mathrm{Re}(k_{zeff})}{\mathrm{Im}(k_{zeff})}$ for accumulation layer ITO carrier concentration of $5\times10^{20}/cm^3$, $2.5\times10^{21}/cm^3$ and $7.5\times10^{21}/cm^3$, for TM polarized bulk modes. As can be seen from Fig. 5a, active modulation of the ITO accumulation layer yields drastic changes in the metamaterial FOM. The "valleys" and "ridges" of Fig. 5a are reproduced in Fig 5b, where we display explicitly the dependence of the normal complex wavenumber supported in the metamaterial for various carrier concentrations in the ITO accumulation layer, extracted from Eq. (1). As recently discussed in Ref. [60], the valleys and ridges of the imaginary part of the wave vector are a good criterion for identifying regions of enhanced and suppressed density of optical states respectively. However, we note that HMMs support high-k modes, so a large imaginary part of the wavenumber may not necessarily imply a reflective region with vanishing density of optical states, if not accompanied by a vanishing real part of the wavenumber. Thus, we include the real part of the wavenumber in the diagrams of Fig. 5b.

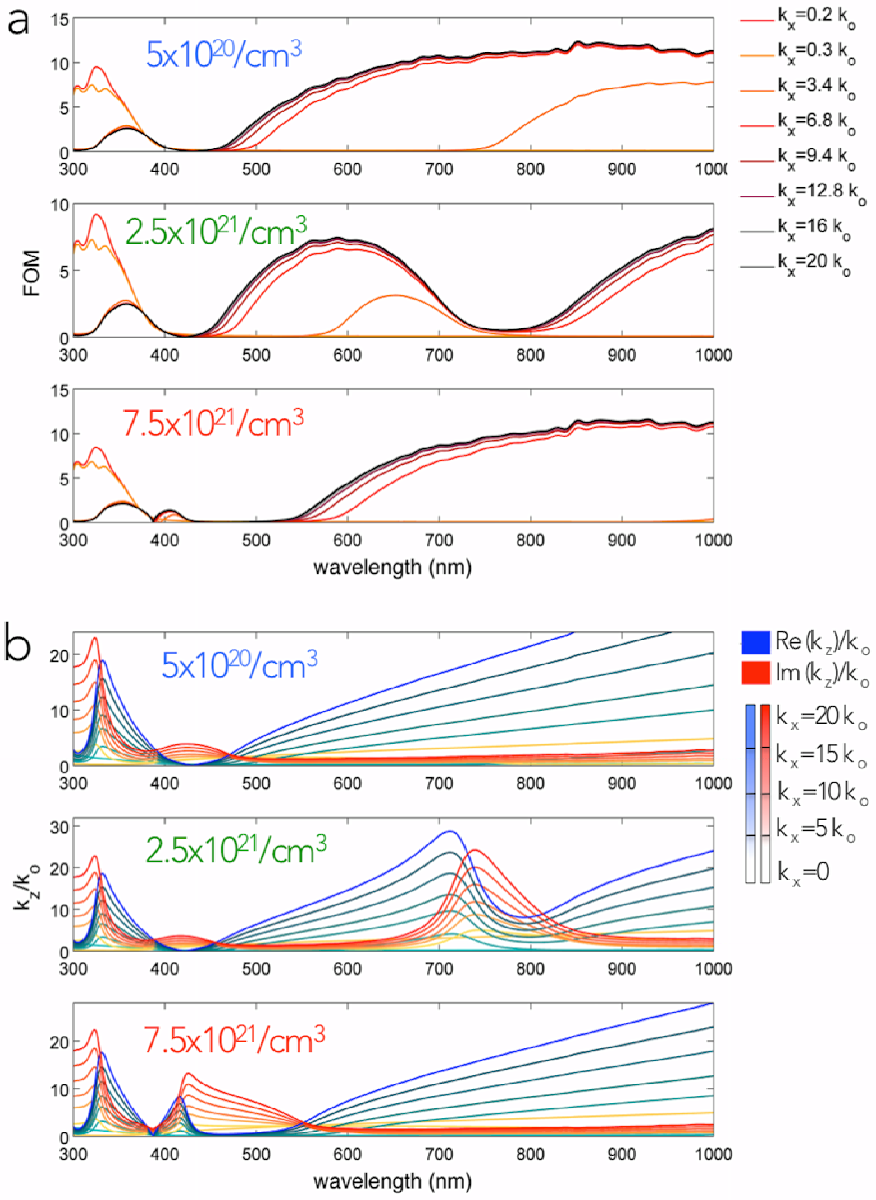

Fig. 5: a: Figure of merit for three different carrier concentrations in the ITO accumulation, b: Real (blue) and imaginary (red) part of effective normal k-vector in the hyperbolic metamaterial, for three different carrier concentrations in the accumulation layer

At a voltage of 0V (carrier concentration being $5\times10^{20}\ /\ cm^3$) the metamaterial supports three distinct spectral regions, as shown in Fig. 5b, top. In the short wavelength regime between 300nm and 400nm, the real part of the wavenumber exceeds the imaginary part, leading to type I hyperbolic dispersion. This region adjoins one in which no photonic states are supported, corresponding to an omnidirectional reflective band gap and suppressed density of states. In this regime, the real parts of both parameters $\varepsilon_o\mu_o$ and $\varepsilon_e\mu_o$ of Eq. (1) have negative values, thus, the real part of the wavenumber

vanishes while the imaginary part is drastically increased. The long wavelength regime exhibits type II hyperbolic dispersion region, as expected for planar HMMs. However, the situation is substantially altered when the carrier concentration increases. As depicted in the bottom two plots of Fig. 5b, the topology of the curves representing both real and imaginary parts of the wavenumber are strongly influenced by the carrier concentration change in the ITO accumulation layer. A new effective band gap is introduced in the longer wavelength limit between 740nm and 810nm for carrier concentration of $2.5\times10^{21}/cm^3$. This is a direct consequence of the introduction of a secondary resonance in the extraordinary permittivity $\mathrm{Re}(\varepsilon_e)$ -(c.f., Fig. 2). This band gap is then drastically blue-shifted for higher ($7.5\times10^{21}/cm^3$ case) accumulation carrier concentration. This is accompanied by strong suppression of the central hyperbolic region. The figure of merit (FOM) of Fig. 5a reaches values as high as 15 for the hyperbolic regions in the hyperbolic dispersion regions. This value largely exceeds the typically observed FOMs which are reported to range between 1-3 for other metamaterial types [61], highlighting the potential of a hyperbolic dispersion for useful, physically realizable metamaterials without excessive losses [62]. By contrast, the FOM vanishes within the band gaps. It is evident from Fig. 5 that use of the field effect enables actively controllable large variations of the HMM FOM ranging between 0-15.

The tunable optical parameters for this metamaterial motif also yield changes in the isofrequency contours and topological transitions. In Fig. 6, we present the complex isofrequency contours for TM bulk modes. Both k_x and k_z are normalized to the free space wavenumber k_o. Application of DC bias across the HMM unit cell is seen to yield drastic changes in both the shape and type of the dispersion surface. Additionally, the surface area enclosed by the isofrequency contours, which is proportional to the total number of available optical states [63] changes significantly with changes in ITO accumulation layer carrier concentration, yielding a route to active control over the metamaterial optical density of states.

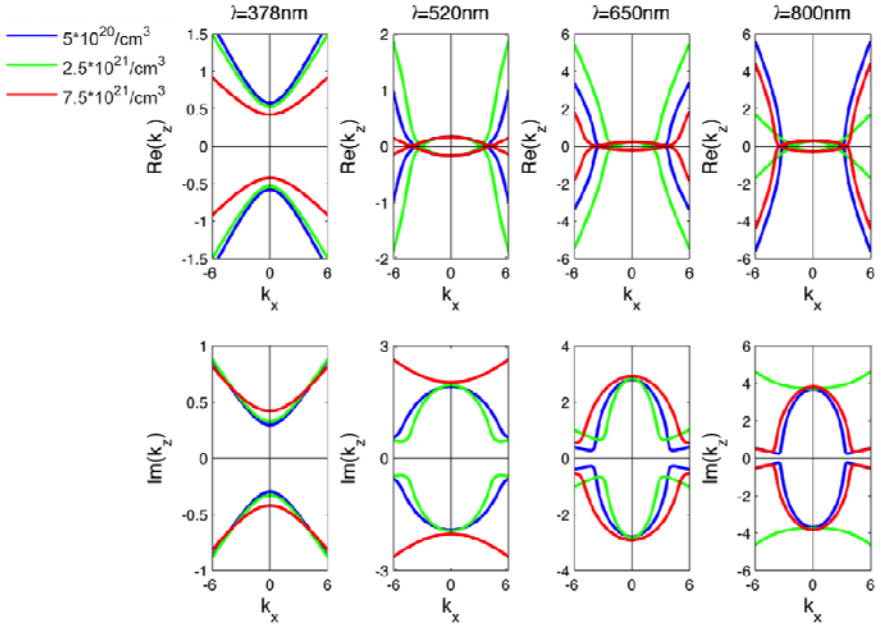

Fig.6: Complex isofrequency contours for three different carrier concentrations in the accumulation layer

As can be seen from Fig. 6, for all the considered free-space wavelengths, the topology of the dispersion surface changes with the ITO carrier density. The isofrequency surfaces at wavelengths of 378nm and 650nm clearly depict regions of type I and type II hyperbolic dispersion, respectively, in agreement to Fig. 5. Hyperbolic dispersion of type I is a consequence of the effective built-in dipole moment in the direction across the optical axis for oblique incidence and TM polarization illumination. Type II hyperbolicity is the result of the metallic response of the metamaterial along the in-plane direction and the dielectric response along the optical axis. Deviations from perfect hyperbolic shapes are expected since the results presented here include losses, which slightly perturb the isofrequency surfaces. For the wavelength of 520nm, it is evident that the area enclosed by the real part of the isofrequency surface for ITO carrier density $7.5x10^{21}/cm^3$ is considerably smaller than for carrier densities $5x10^{20}/cm^3$ and $2.5x10^{21}/cm^3$. Additionally, the losses are clearly higher for this carrier concentration as shown by the red curve of the imaginary part of the isofrequency curve. This wavelength falls in a photonic band gap region for an ITO carrier density of $7.5x10^{21}/cm^3$. At this carrier density, the real parts of both parameters $\varepsilon_o\mu_o$ and $\varepsilon_e\mu_o$ are negative, leading to a forbidden band, as can be seen in Fig. 5. Thus, for this wavelength, the metamaterial experiences a topological transition from a hyperbolic state to a forbidden region with increasing carrier concentration, visible as the abrupt change in the topology of the imaginary part of the red isofrequency surface compared to blue and green ones. For 800nm wavelength, a similar observation can be made for the green curve corresponding to an ITO carrier density of $2.5x10^{21}/cm^3$. For this carrier concentration, the metamaterial exhibits a band gap, as indicated in Fig. 5. In the Appendix, we illustrate the same isofrequency contours in the lossless limit (c.f. Fig. A6). Comparing these results, one can conclude that the hyperbolic dispersion is evident at wavelengths of 378nm and 650nm, while the noted band gaps are also identifiable by the absence of a red curve and a green curve for the wavelengths of 520nm and 800nm respectively, indicating vanishing density of optical states for these wavelengths.

To illustrate the effects of tunable optical parameters on the effective band structure, we show in Fig. 7 the change in the topology of the frequency-dependent three-dimensional dispersion surface for the two extreme cases of ITO accumulation carrier concentration, in the lossless limit.

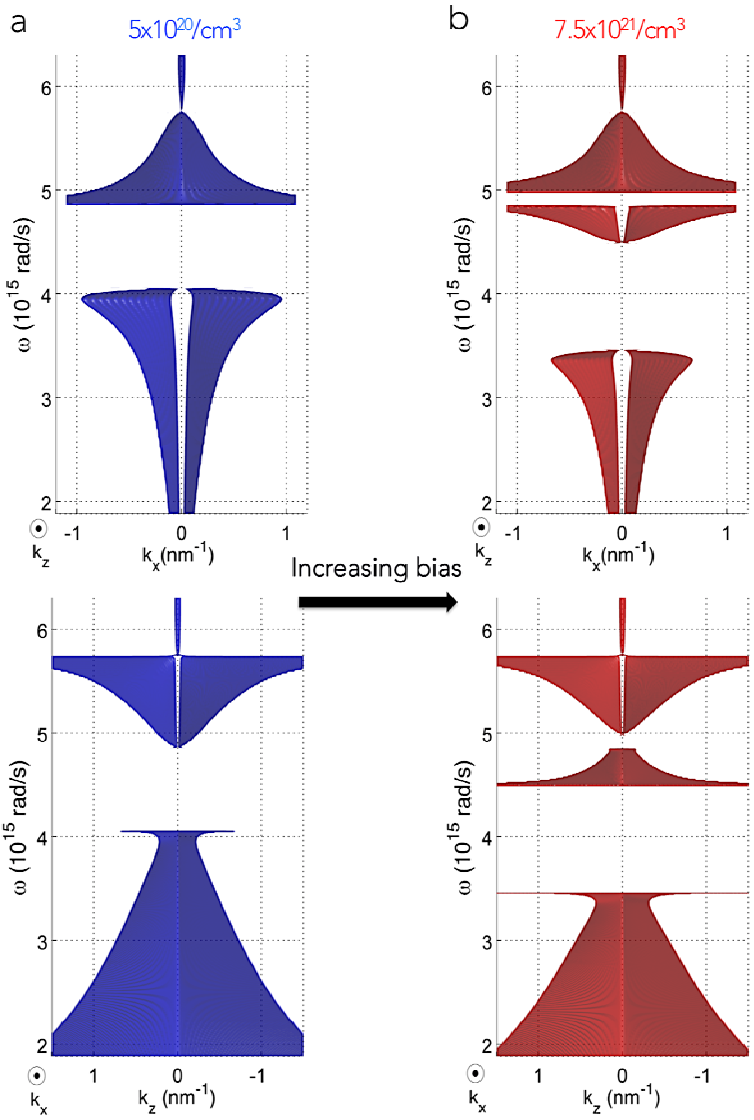

Fig.7: Three-dimensional dispersion surface along k_z axis (top) and along k_x axis (bottom) for carrier concentration in the ITO accumulation layer a) $5\times10^{20}\ /\ cm^3$ corresponding to 0V applied bias and b) $7.5\times10^{21}\ /\ cm^3$

Fig. 7 illustrates the effect of ITO electric permittivity modulation on the metamaterial dispersion surface when applying a DC bias across the Ag-HfO_2-ITO layers. Within the optical regime, we see an effective omnidirectional band gap whose band edges can be tuned by varying the applied bias. Additionally, we notice the appearance of a new effective band gap and a new hyperbolic region, for larger accumulation layer carrier concentration changes. This reveals that the field effect provides sufficient change of the conductive oxide permittivity to allow for spectral shifting of the hyperbolic regions and band gaps of HMMs and even to allow for active "opening" and "closing" of band gaps.

C. Sensitivity analysis over TCO electronic parameters

As shown in Eq. (2), the parameter that principally defines the tunability range of the effective optical parameters of our metamaterial is the product $N\cdot d$, where N is the maximum achievable carrier concentration in the accumulation layer of the TCO before electrical breakdown occurs, and d is

the Debye length or thickness of the accumulation layer. We perform a sensitivity analysis of the retrieved extraordinary permittivity ε_e, separately as a function of N and d, since ε_e is the optical parameter most drastically affected by the field effect. Both for N and d, we consider values within the range of previous experimental reports [32-34, 39, 40, 41]. We suggest that this approach can provide useful insight here, and also for other semiconductors and TCOs as active constituent materials in field-effect-tunable metamaterial realizations. In Fig. 8 we illustrate the tunability of the ENP region of the primary Lorentzian resonance.

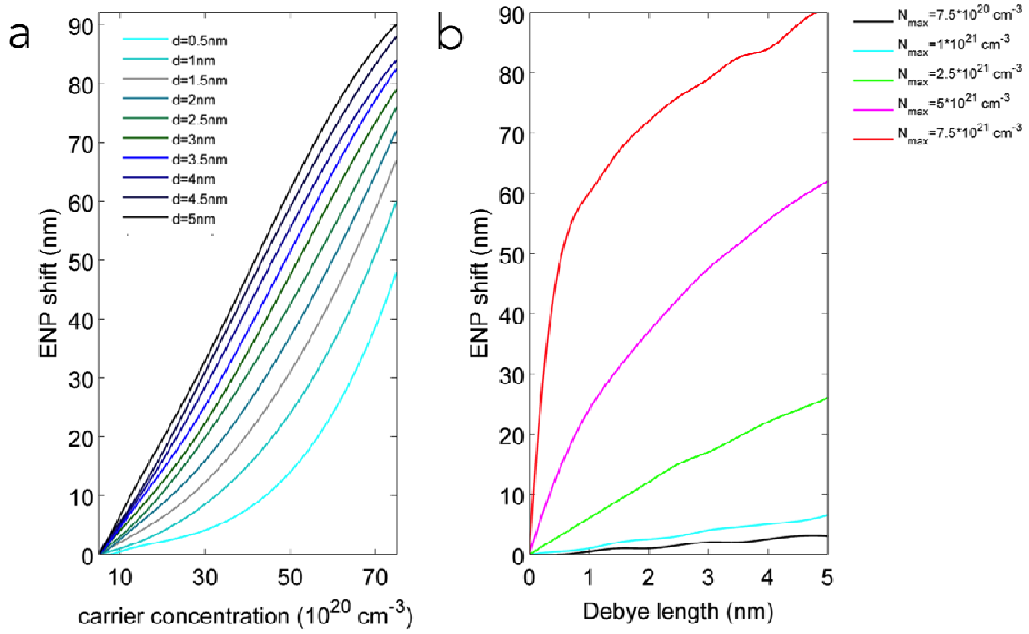

Fig.8: Effects of the electronic properties of ITO on the ENP wavelength of ε_e. a) carrier concentration change effect for varying Debye lengths b) Debye length effect for varying maximum achievable carrier concentration in the accumulation layer before breakdown occurs

The maximum achievable change in the carrier concentration of the accumulation layer before breakdown occurs is a critical factor for the ENP shift, as shown in Fig. 8a. Specifically, for experimentally realizable TCOs [32, 33, 38, 39] that have been shown to undergo large changes in carrier concentration, the wavelength shift is large enough to be experimentally detectible. Tunability of the ENP wavelength for metamaterials that undergo an elliptical to hyperbolic transition, should give rise to readily observable changes in photoluminescence [64] or cathodoluminescence [65, 66] intensities.

As indicated from Fig. 2, it is the appearance of secondary resonances in ε_e, upon application of DC bias across the metamaterial layers that has the strongest effect on tuning the birefringence, dichroism and effective band structure of the metamaterial. To investigate this, we calculate below the effect of the Debye thickness and maximum achievable carrier concentration change on the relative change of the real part of ε_e, $\left|\Delta\varepsilon_e\right|_{rel} = \left|\dfrac{\varepsilon_e(0V) - \varepsilon_e}{\varepsilon_e(0V)}\right|$ under applied bias.

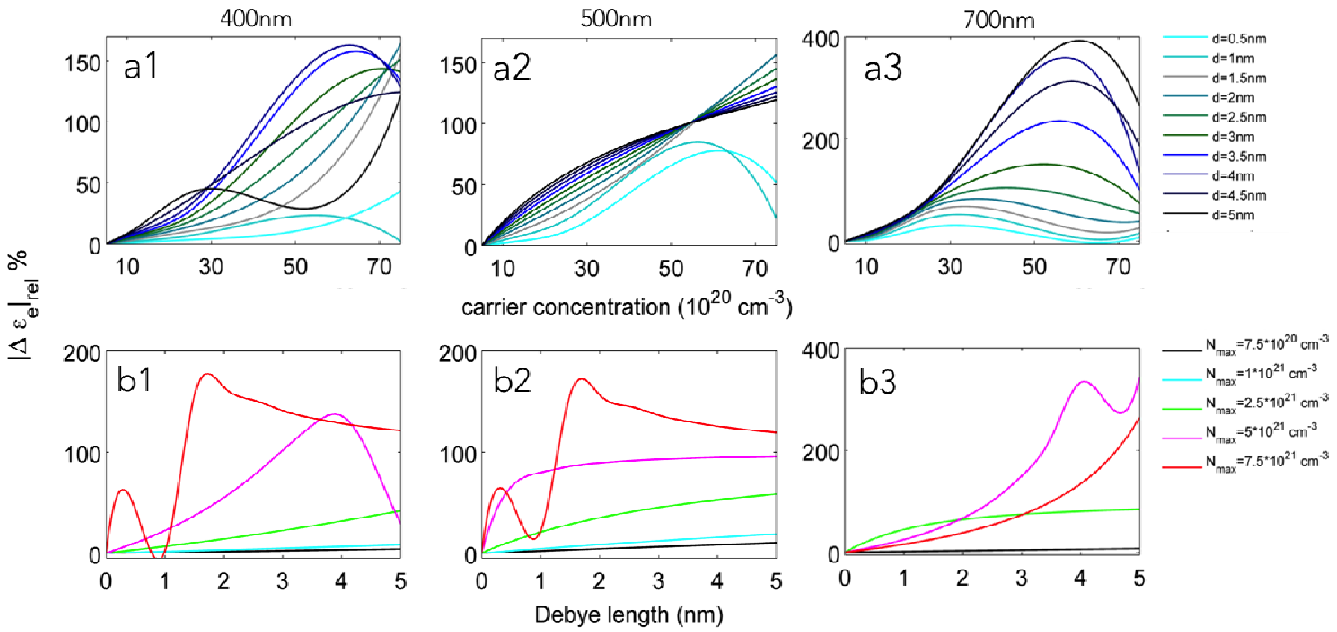

Fig.9: Variation in the electronic properties of ITO and their effect on relative change of ε_e .Top: carrier concentration change effect for varying Debye lengths for wavelengths of a1) 400nm, a2) 500nm, a3) 700nm and bottom: Debye length effect for varying maximum achievable carrier concentration in the accumulation layer before breakdown occurs for b1) 400nm, b2) 500nm, b3) 700nm

As shown in Figs. 9, a1, 2 and 3, even for Debye lengths in the order of 0.5nm, the relative change in the value of ε_e is of the order of 20%-100% for the wavelengths accessed here. This large change arises from the appearance of secondary resonances in ε_e. Figs. 9, b1, 2, and 3 suggest that achieving very high carrier densities in the accumulation layer of the TCO facilitates the strong, experimentally observable tunability effects. For example, as seen from the red and magenta curves in Figs. 9 b1, 2, 3, the relative change $\left|\Delta\varepsilon_e\right|_{rel}$ can be as high as 150%-350% for a 100x modulation of the TCO accumulation carrier density.

III. CONCLUSION

In conclusion, we have outlined a method for electronically tuning the topology of the dispersion surface of hyperbolic metamaterials by field-effect gating and electrical modulation of the permittivity in transparent conductive oxide layers. We observe the "opening" and "closing" of omnidirectional band gaps controlled by applied bias, which corresponds to a tunable figure of merit, with FOM values as high as 15 in the hyperbolic regime while vanishing at the band gaps. The field-effect induced changes in the permittivity of the TCO accumulation layers give rise to spectral tunability of the effective parameters of hyperbolic metamaterials. We observe blue shifts of the effective permittivity along the optical axis by more than 60nm in the visible regime and additional resonances are introduced due to the large changes in carrier density across metal-dielectric-TCO triplet layers. This gives rise to broadband tunability of the effective birefringence and dichroism, with potential for novel photonic devices like tunable metal-dielectric waveguides, optical sensors, filters and polarizers. Such active control over the complex parameters of metamaterials is also essential for slow light media and holographic displays. A sensitivity analysis of the extraordinary permittivity to changes in the TCO carrier concentration and accumulation

layer thickness indicates the robustness of field effect modulation as a tuning mechanism. The straightforward fabrication of multilayer metamaterials by thin film deposition techniques suggests that the experimental realization of tunable field effect metamaterials with tunable optical parameters is well within reach.

Acknowledgments

This work was supported by U.S. Department of Energy (DOE) Office of Science grant DE-FG02-07ER46405 (G.P. and H.A.A.). G. Papadakis acknowledges support by a National Science Foundation Graduate Research Fellowship. We acknowledge fruitful discussions with Prof. Pochi Yeh, Dr. Ho W. Lee, Dr. Krishnan Thyagarajan, Dr. Salvatore Campione and Prof. E. N. Economou.

Author Information

Corresponding author email: gpapadak@caltech.edu

Notes: The authors declare no competing financial interest

Appendix

A1. LOCALITY OF EFFECTIVE EXTRACTED PARAMETERS

In order to investigate on the locality of the effective parameters, we present in Fig. A1 the extracted extraordinary parameters ε_e and μ_e of the considered unit cell metamaterial, for ITO carrier concentration in both accumulation and bulk regions being $5\times10^{20}/cm^3$, using the retrieval technique of Ref.[1], for different incident angles. It is noted here that, as proved in Ref.[1], the ordinary parameters ε_o and μ_o are only valid for normal incidence and thus, they cannot serve as a metric of locality.

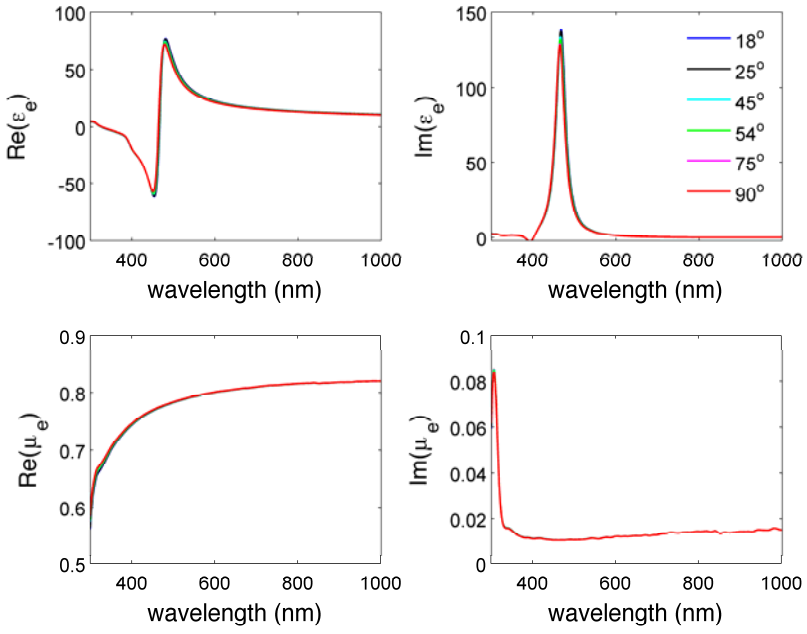

Fig.A1: Angle independence of effective extraordinary parameters for carrier concentration $5\times10^{20}/cm^3$

It can be seen from Fig.A1 that for all the considered incident angles, the extraordinary parameters converge to the same curves. The angle independence of ε_e and μ_e implies their independence on the wave vector, and thus, their locality. We obtain similar, angle independent parameters for all the consider carrier concentrations in the ITO accumulation layers. The locality of the effective parameters indicates that a large number of unit cell HMMs stacked together yields similar effective parameters to the original unit cell.

A2. Comparison to Bloch method

As discussed in the main text, in order to verify the dispersion characteristics of the metamaterial, we compare below the dispersion relation for the unit cell metamaterial presented in Fig. 1, calculated through the utilized retrieval method [1] to the dispersion of an infinite stack of unit cells, calculated through the generalized Bloch wave vector. Specifically, the unit cell of Fig. 1 is not a periodic alteration of only two constituent materials. Thus, the general Bloch wave-vector method for layered media [67] cannot be directly applied. Instead, we use the generalized image parameter method [59] which can be applied for any type of unit cell.

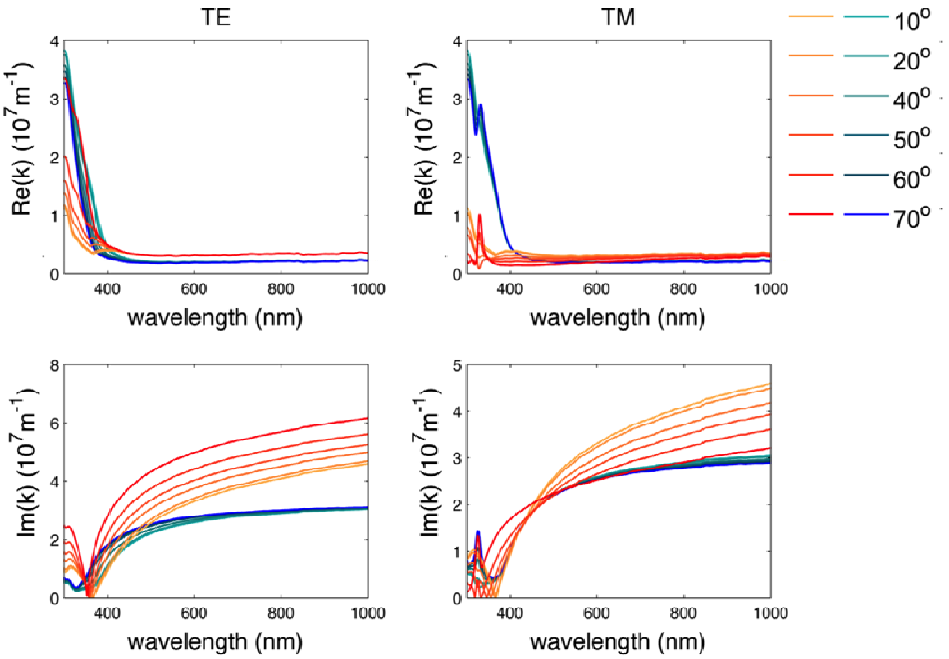

Fig.A2: Comparison between Bloch-wave vector (red-colored curves) for an infinite stack of unit cell metamaterial to retrieval results [1] (blue-colored curves) for ITO carrier concentration in the accumulation layer $5\text{x}10^{20}/\text{cm}^3$ for different incident angles

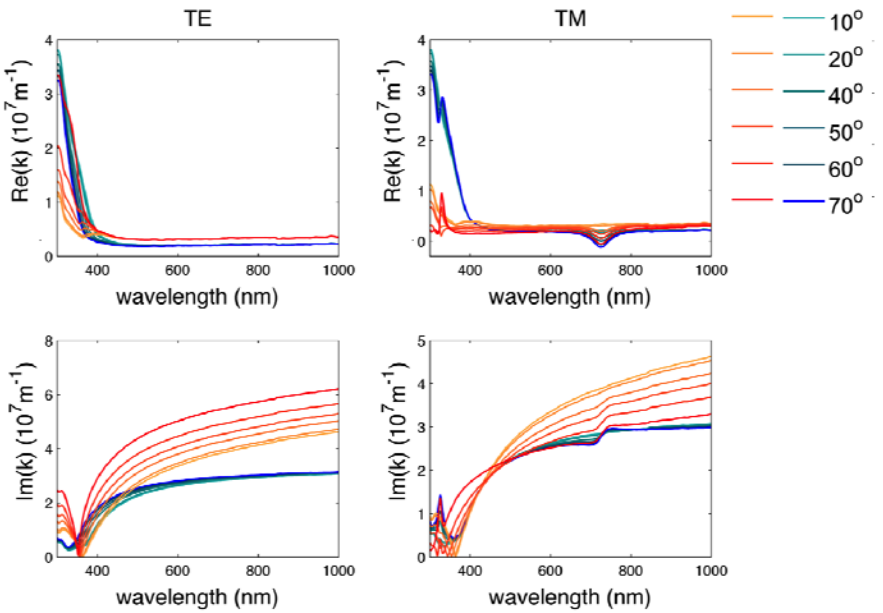

Fig.A3: Comparison between Bloch-wave vector (red-colored curves) for an infinite stack of unit cell metamaterial to retrieval results [1] (blue-colored curves) for ITO carrier concentration in the accumulation layer $2.5\text{x}10^{21}/\text{cm}^3$ for different incident angles

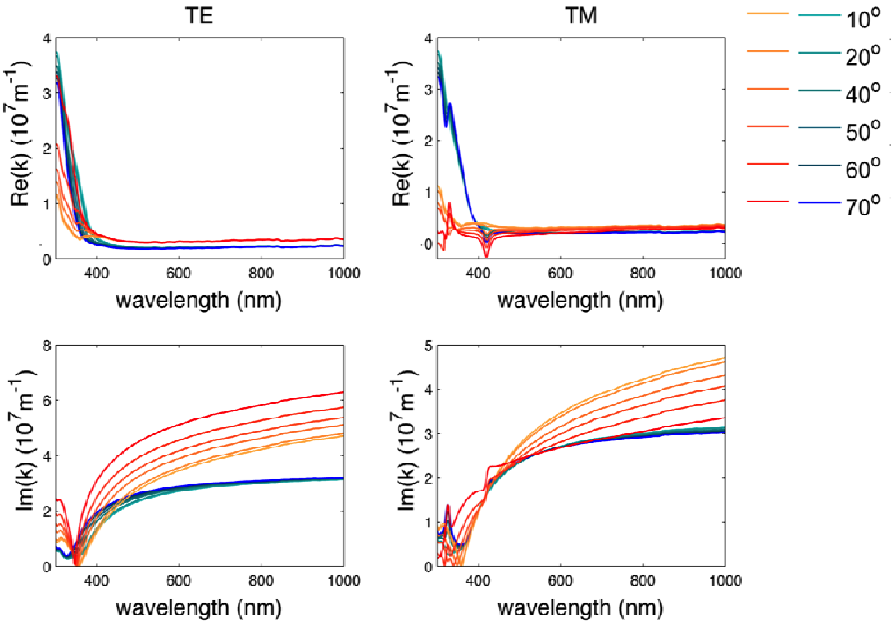

Fig.A4: Comparison between Bloch-wave vector (red-colored curves) for an infinite stack of unit cell metamaterial to retrieval results [1] (blue-colored curves) for ITO carrier concentration in the accumulation layer $7.5\text{x}10^{21}/\text{cm}^3$ for different incident angles

Deviations of the Bloch theory results from the retrieval results are expected since, for a stack of just $a = 70nm$, which is the total thickness of the metamaterial unit cell under study, edge effects

(terminating layers), thickness effects and layer sequence effects that the Bloch-theory neglects become important (See Ref. [1] for more details). However, as can be seen from Figs. A2, 3, 4, all characteristic trends of the wave-vectors curves match in the two pictures: Bloch-theory infinite stack and unit-cell retrieval calculations. The losses, in other the imaginary parts of the wave-vector, are increased in the Bloch-theory picture, as expected since in the Bloch-picture the stack is infinitely periodic, yielding higher losses. Additionally, in the long wavelength regime, the real part of the wave-vectors, for both polarization, agree very well with the retrieval calculations, which indicates the accuracy and locality of the retrieved effective parameters (as verified in Fig. A1). In the shorter wavelength regime, the disagreement becomes more evident for TM polarization. However, by closely examining the wavelength range of 300nm-400nm in Figs. A2-4 for TM polarization, it is evident that the offset difference between the Bloch theory and retrieval results is close to π / a , where $a = 0.7 \times 10^{-7} m$ is the total thickness of the metamaterial unit cell. Thus, those wave-vectors yield approximately equal phases for TM polarized waves propagating in the metamaterials.

A3. TUNABILITY OF ε_o

We present in Fig. A5 the wavelength dependence of the ordinary permittivity ε_o as the carrier concentration of the accumulation layer ITO increases, for the geometry of Fig. 1.

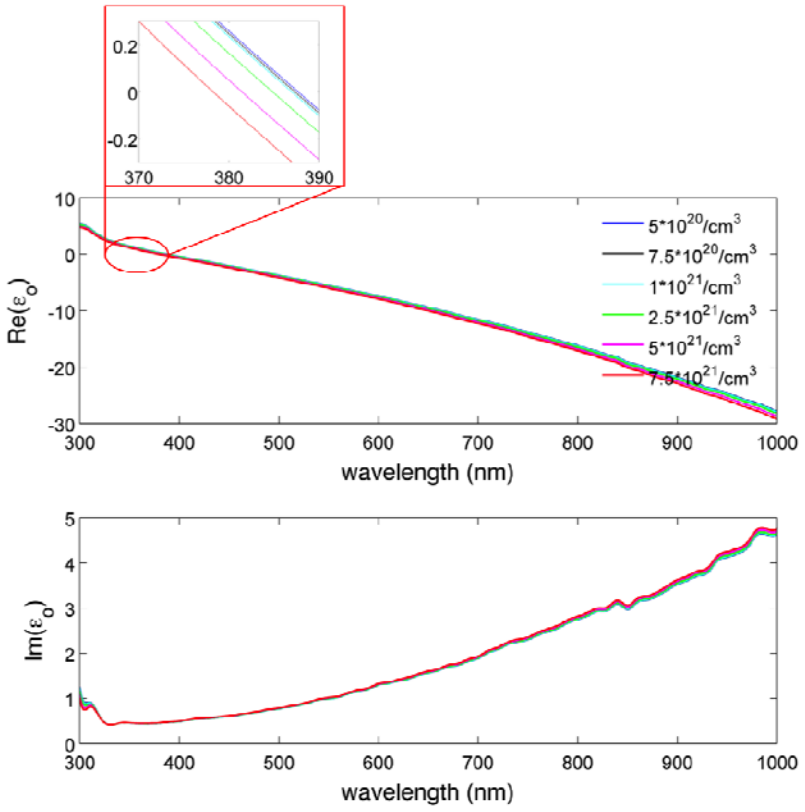

Fig. A5: Effective ordinary permittivity. Top: real part and bottom: imaginary part of ε_o for various carrier concentrations in the accumulation layer

The ordinary permittivity does not exhibit considerable spectral shifting as the carrier

concentration increases, which is expected since the Drude-like response in the in-plane direction is mostly affected by the presence of Ag. However, the inset shows tunability in the order of some nanometers of the ENZ wavelength of ε_o which is sufficient for inducing considerable changes in the metamaterial optical response from dielectric-like to metallic-like for TE polarized modes.

A4. Isofrequency contours in the lossless limit

Regarding the isofrequency curves presented in Fig. 6 of the main text, we show below the equivalent calculation in the lossless limit. Difference in the shapes corresponding to different carrier concentration in the ITO accumulation layer reveal the potential of actively controlling this metamaterial's density of optical states.

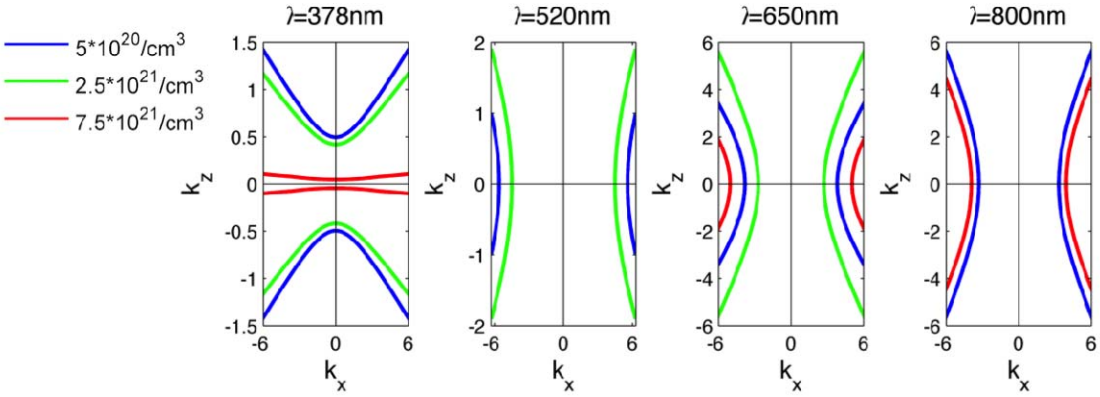

Fig. A6: Isofrequency contours for three different carrier concentrations in the lossless limit

As verified in the main text in Figs. 5 and 6, the wavelengths of 378nm and 650nm experience hyperbolic dispersion of type I and II, respectively. To the contrary, the absence of an isofrequency contour for ITO carrier concentration $7.5x10^{21}/cm^3$ (red curve) for the wavelength of 520nm and for ITO carrier concentration $2.5x10^{21}/cm^3$ (green curve) for the wavelength of 800nm reveal the existence of an omnidirectional band gap and vanishing density of states for these wavelengths and carrier concentrations. The existence of both band gaps is verified by Figs. 5 and 6 in the main text.

References

1 G. T. Papadakis, P. Yeh, and H. A. Atwater, Physical Review B **91**, 155406 (2015).
2 N. Engheta, Science **340**, 286 (2013).
3 R. Maas, J. Parsons, N. Engheta, and A. Polman, Nat Photon **7**, 907 (2013).
4 A. M. Mahmoud and N. Engheta, Nat Commun **5** (2014).
5 J. B. Pendry, Physical Review Letters **85**, 3966 (2000).
6 R. Z. N. Engheta, *Physics and Engineering Explorations* 2006).
7 M. Choi, et al., Nature **470**, 369 (2011).
8 A. Poddubny, I. Iorsh, P. Belov, and Y. Kivshar, Nat Photon **7**, 948 (2013).
9 A. V. Shchelokova, D. S. Filonov, P. V. Kapitanova, and P. A. Belov, Physical Review B **90**, 115155 (2014).
10 D. Lu, J. J. Kan, E. E. Fullerton, and Z. Liu, Nat Nano **9**, 48 (2014).

11 J. Zhou, A. F. Kaplan, L. Chen, and L. J. Guo, ACS Photonics **1**, 618 (2014).
12 M. Esslinger, R. Vogelgesang, N. Talebi, W. Khunsin, P. Gehring, S. de Zuani, B. Gompf, and K. Kern, ACS Photonics **1**, 1285 (2014).
13 S. N. Khan and D. D. Johnson, Physical Review Letters **112**, 156401 (2014).
14 M. Neupane, et al., Nat Commun **5** (2014).
15 Y. L. Chen, et al., Science **325**, 178 (2009).
16 M. C. Rechtsman, J. M. Zeuner, Y. Plotnik, Y. Lumer, D. Podolsky, F. Dreisow, S. Nolte, M. Segev, and A. Szameit, Nature **496**, 196 (2013).
17 A. B. Khanikaev, S. Hossein Mousavi, W.-K. Tse, M. Kargarian, A. H. MacDonald, and G. Shvets, Nat Mater **12**, 233 (2013).
18 W. Gao, M. Lawrence, B. Yang, F. Liu, F. Fang, B. Béri, J. Li, and S. Zhang, Physical Review Letters **114**, 037402 (2015).
19 Y. Li and J. Mei, Opt. Express **23**, 12089 (2015).
20 X. Huang, Y. Lai, Z. H. Hang, H. Zheng, and C. T. Chan, Nat Mater **10**, 582 (2011).
21 W. N. Yu Guo, Cristian L. Cortes, and Zubin Jacob, Advances in OptoElectronics **2012** (2012).
22 H. N. S. Krishnamoorthy, Z. Jacob, E. Narimanov, I. Kretzschmar, and V. M. Menon, Science **336**, 205 (2012).
23 I. V. Iorsh, I. S. Mukhin, I. V. Shadrivov, P. A. Belov, and Y. S. Kivshar, Physical Review B **87**, 075416 (2013).
24 M. A. K. Othman, C. Guclu, and F. Capolino, Opt. Express **21**, 7614 (2013).
25 A. Madani, S. Zhong, H. Tajalli, S. Roshan Entezar, and a. Y. M. A. Namdar, Progress In Electromagnetics Research **143**, 545 (2013).
26 A. Leviyev, B. Stein, T. Galfsky, H. Krishnamoorthy, I. L. Kuskovsky, V. Menon, and A. B. Khanikaev, arxiv:150505438[physics.optics] (2015).
27 M. J. Dicken, K. Aydin, I. M. Pryce, L. A. Sweatlock, E. M. Boyd, S. Walavalkar, J. Ma, and H. A. Atwater, Opt. Express **17**, 18330 (2009).
28 J.-Y. Ou, E. Plum, J. Zhang, and N. I. Zheludev, Nat Nano **8**, 252 (2013).
29 Y. Gong, Z. Li, J. Fu, Y. Chen, G. Wang, H. Lu, L. Wang, and X. Liu, Opt. Express **19**, 10193 (2011).
30 D. Kalavrouziotis, et al., Opt. Express **20**, 7655 (2012).
31 J. P. Turpin, J. A. Bossard, K. L. Morgan, D. H. Werner, and P. L. Werner, International Journal of Antennas and Propagation **2014**, 18 (2014).
32 E. Feigenbaum, K. Diest, and H. A. Atwater, Nano Letters **10**, 2111 (2010).
33 H. W. Lee, G. Papadakis, S. P. Burgos, K. Chander, A. Kriesch, R. Pala, U. Peschel, and H. A. Atwater, Nano Letters **14**, 6463 (2014).
34 L. Zhaolin, Z. Wangshi, and S. Kaifeng, Photonics Journal, IEEE **4**, 735 (2012 and references therein).
35 S. Zhu, G. Q. Lo, and D. L. Kwong, Opt. Express **21**, 8320 (2013).
36 V. E. Babicheva, N. Kinsey, G. V. Naik, M. Ferrera, A. V. Lavrinenko, V. M. Shalaev, and A. Boltasseva, Opt. Express **21**, 27326 (2013).
37 G. V. Naik, J. Kim, and A. Boltasseva, Opt. Mater. Express **1**, 1090 (2011).
38 A. Boltasseva and H. A. Atwater, Science **331**, 290 (2011).
39 X. Liu, J. Park, J.-H. Kang, H. Yuan, Y. Cui, H. Y. Hwang, and M. L. Brongersma, Applied Physics Letters **105**, 181117 (2014).

[40] F. Yi, E. Shim, A. Y. Zhu, H. Zhu, J. C. Reed, and E. Cubukcu, Applied Physics Letters **102**, 221102 (2013).

[41] A. P. Vasudev, J.-H. Kang, J. Park, X. Liu, and M. L. Brongersma, Opt. Express **21**, 26387 (2013).

[42] F. Michelotti, L. Dominici, E. Descrovi, N. Danz, and F. Menchini, Opt. Lett. **34**, 839 (2009).

[43] D. Mergel and Z. Qiao, Journal of Physics D: Applied Physics **35**, 794 (2002).

[44] C. Sire, S. Blonkowski, M. J. Gordon, and T. Baron, Applied Physics Letters **91**, 242905 (2007).

[45] C. M. Tanner, Y.-C. Perng, C. Frewin, S. E. Saddow, and J. P. Chang, Applied Physics Letters **91**, 203510 (2007).

[46] Z. C. Y. a. P. K. C. A. P. Huang, Advances in Solid State Circuit Technologies (2010).

[47] M. D. Groner, J. W. Elam, F. H. Fabreguette, and S. M. George, Thin Solid Films **413**, 186 (2002).

[48] J. Yota, H. Shen, and R. Ramanathan, Journal of Vacuum Science & Technology A **31**, 01A134 (2013).

[49] J. Robertson, The European Physical Journal Applied Physics **28**, 265 (2004).

[50] F. R. Z. M. Rittersma, M. A. Verheijen,b J. G. M. van Berkum,, b. J. H. M. S. T. Dao, E. Vainonen-Ahlgren,E. Tois,M. Tuominen,and, and S. Haukka, J. Electrochem. Soc. **151** (2004).

[51] F. M. Li, B. C. Bayer, S. Hofmann, J. D. Dutson, S. J. Wakeham, M. J. Thwaites, W. I. Milne, and A. J. Flewitt, Applied Physics Letters **98**, 252903 (2011).

[52] Y. H. Kim, K. Onishi, C. S. Kang, H.-J. Cho, R. Choi, S. Krishnan, M. S. Akbar, and J. C. Lee, Electron Device Letters, IEEE **24**, 40 (2003).

[53] A. Taube, S. Gierałtowska, T. Gutt, T. Małachowski, I. Pasternak, T. Wojciechowski, W. Rzodkiewicz, M. Sawicki, and A. Piotrowska, Acta Physica Polonica, A. **119**, 696 (2011).

[54] W.-J. Yoon and P. R. Berger, Organic Electronics **11**, 1719 (2010).

[55] W. Mao, et al., Chinese Physics B **20**, 097203 (2011).

[56] C.-S. Pang and J.-G. Hwu, Nanoscale Research Letters **9** (2014).

[57] See supplemental Material at [] for optical constants of Ag and ITO.

[58] D. L. Wood, K. Nassau, T. Y. Kometani, and D. L. Nash, Applied Optics **29**, 604 (1990).

[59] D. M. Pozar, *Microwaves Engineering*, 2012).

[60] E. E. Narimanov, Physical Review X **4**, 041014 (2014).

[61] G. Dolling, C. Enkrich, M. Wegener, C. M. Soukoulis, and S. Linden, Opt. Lett. **31**, 1800 (2006).

[62] A. J. Hoffman, L. Alekseyev, S. S. Howard, K. J. Franz, D. Wasserman, V. A. Podolskiy, E. E. Narimanov, D. L. Sivco, and C. Gmachl, Nat Mater **6**, 946 (2007).

[63] Z. Jacob, J. Y. Kim, G. V. Naik, A. Boltasseva, E. E. Narimanov, and V. M. Shalaev, Applied Physics B **100**, 215 (2010).

[64] Thin Solid Films **496**, 520 (2006).

[65] T. Coenen, E. J. R. Vesseur, and A. Polman, Applied Physics Letters **99**, 143103 (2011).

[66] M. Kuttge, W. Cai, F. J. García de Abajo, and A. Polman, Physical Review B **80**, 033409 (2009).

[67] P. Yeh, *Optical Waves in Layered Media* (Wiley Series in Pure and Applied OptIcs, Canada, Hoboken, New Jersey, 1988).